Front. Earth Sci. 2018, 12(3): 481–490
https://doi.org/10.1007/s11707-017-0681-9

RESEARCH ARTICLE

Quantitative extraction of the bedrock exposure rate based on unmanned aerial vehicle data and Landsat-8 OLI image in a karst environment

Hongyan WANG, Qiangzi LI (✉), Xin DU, Longcai ZHAO

Institute of Remote Sensing and Digital Earth, Chinese Academy of Sciences, Beijing 100101, China

Abstract In the karst regions of southwest China, rocky desertification is one of the most serious problems in land degradation. The bedrock exposure rate is an important index to assess the degree of rocky desertification in karst regions. Because of the inherent merits of macro-scale, frequency, efficiency, and synthesis, remote sensing is a promising method to monitor and assess karst rocky desertification on a large scale. However, actual measurement of the bedrock exposure rate is difficult and existing remote-sensing methods cannot directly be exploited to extract the bedrock exposure rate owing to the high complexity and heterogeneity of karst environments. Therefore, using unmanned aerial vehicle (UAV) and Landsat-8 Operational Land Imager (OLI) data for Xingren County, Guizhou Province, quantitative extraction of the bedrock exposure rate based on multi-scale remote-sensing data was developed. Firstly, we used an object-oriented method to carry out accurate classification of UAV images. From the results of rock extraction, the bedrock exposure rate was calculated at the 30 m grid scale. Parts of the calculated samples were used as training data; other data were used for model validation. Secondly, in each grid the band reflectivity of Landsat-8 OLI data was extracted and a variety of rock and vegetation indexes (e.g., NDVI and SAVI) were calculated. Finally, a network model was established to extract the bedrock exposure rate. The correlation coefficient of the network model was 0.855, that of the validation model was 0.677 and the root mean square error of the validation model was 0.073. This method is valuable for wide-scale estimation of bedrock exposure rate in karst environments. Using the quantitative inversion model, a distribution map of the bedrock exposure rate in Xingren County was obtained.

Received July 6, 2017; accepted October 8, 2017

E-mail: liqz@radi.ac.cn

Keywords bedrock exposure rate, quantitative extraction, UAV and Landsat-8 OLI data, karst rocky desertification

1 Introduction

Karst regions are typically ecologically fragile zones constrained by their geological setting, with poor environmental and anti-interference ability (Yue et al., 2012). Karst has a wide distribution globally, with southwest China being a typical area. In the karst regions of southwest China, rocky desertification is a special kind of land-degradation process in which soil and water are seriously eroded, bedrock is widely exposed, and the carrying capability of the land markedly declines; finally, the degraded karst landscape appears similar to desert. Karst rocky desertification has become one of the most serious ecological and environmental problems in China, followed by sandy desertification in northwest China and soil and water erosion in the Loess Plateau (Wang and Li, 2007; Jiang et al., 2014; Dai et al., 2017; You, 2017).

Karst rocky desertification is one of the most serious problems in land degradation. The bedrock exposure rate and fractional cover of green vegetation are the main surface features and key ecological indicators of karst rocky desertification (Yue et al., 2011). Remote sensing can be used to quantify ecological indicators for assessment of karst rocky desertification. Vegetation indices, which are defined on the basis of the spectral features of green vegetation, can be used to extract vegetation information. Much previous research has focused on constructing image-based indices to retrieve the vegetation and micrometeorological conditions of the land surface to monitor karst rocky desertification at different scales (Runnström, 2003; Geerken and Ilaiwi, 2004; Zhang et al., 2011; Xu and Zhang, 2014; Zhang et al., 2014; Tavares et al., 2015; Salvati et al., 2016). However, the accuracy of

the bedrock exposure rate acquired from satellite images is variable (Lagacherie et al., 2008). In previous studies, a rock index based on the spectral reflectance of rock was defined and quantitative extraction of the bedrock exposure rate was based on a linear model of rock index or the dimidiate pixel model of rock index. The most popular one applied in karst environment may be the karst rocky desertification synthesis index (KRDSI). KRDSI, which derived from narrow shortwave infrared bands (2000–2400 nm), is only deployed on hyperspectral images. Narrow shortwave infrared bands are generally not available on low-cost multispectral sensors. The accuracy of these models was not high, and the models were not suitable for a wide range of applications (Yang et al., 2012; Xiong et al., 2013; Zong et al., 2014). In order to accurately estimate land cover fractions in karst areas, particularly at subpixel scale, spectral mixture analysis (SMA) was often used. Although the SMA algorithms are physical based approaches and able to acquire subpixel endmember fractions effectively, it is extremely difficult to apply in a large geographic area because of the difficulties in endmember selection and intraclass variability quantification (Xie et al., 2015; Zhang et al., 2017).

It is well known that the ground surface is broken and that the ground objects are complex in karst areas. Actual measurement of the bedrock exposure rate is difficult and the calculation of bare rock area is uncertain. The present remote-sensing methods cannot directly be exploited to extract the rate of exposed bedrock owing to the high complexity and heterogeneity of karst environments (Yue et al., 2011). Therefore, using unmanned aerial vehicle (UAV) and Landsat-8 OLI data, the paper selected Xingren County as the research area, and a method for quantitative extraction of the bedrock exposure rate using multi-scale remote-sensing data was developed. This method will solve the two major problems: one is the true value measurement of bedrock exposure rate and the other is the large scale rocky desertification assessment in karst areas.

2 Study area

Xingren County, which is located in southwest Guizhou Province, is one of the more seriously rocky desertified counties in the province. The study area covers the region from 25°16′N and 104°54′E to 25°48′N and 105°34′E. The total area is 1785 km^2, of which 1282 km^2 (71.8%) is karst. Xingren County consists low mountain landforms and suffers from erosion and gully development. The terrain is high in the west, low in the east. The highest elevation is 2014 m and the lowest elevation is 460 m. The most obvious land surface features are the widespread exposure of carbonate rocks and low vegetation cover. Moreover, the variety of complex terrain increases spatial landscape heterogeneity, which appears as discontinuously distributed soil rock and fragmented ecological spaces for vegetation. Land covers here are often mixtures of rock, soil, and vegetation. The region possesses a northern subtropical humid monsoon climate, with an annual average temperature of 15.2°C and annual precipitation of approximately 1325 mm.

3 Data and pre-processing

3.1 Landsat-8 Operational Land Imager data

In this study, one full-spatial-resolution Landsat-8 Operational Land Imager (OLI) image (Path/Row: 128/42) acquired on March 18, 2015 was downloaded from the United States Geological Survey (USGS) website. Landsat-8 was designed by the National Aeronautics and Space Administration (NASA) and was launched on 11 February 2013 carrying the OLI and the Thermal Infrared Sensor. The satellite was subsequently transferred to USGS for routine operations (Roy et al., 2014). The image was level-1 processed, i.e., it underwent system radiation correction and geometric correction. The Landsat-8 OLI data were processed in two steps: 1) radiance calibration and 2) atmospheric correction. The Landsat-8 OLI image was atmospherically corrected to generate surface reflectance using the Fast Line-of-Sight Atmospheric Analysis of Spectral Hypercubes (Matthew et al., 2000), a mature, easy-to-use atmospheric correction method imbedded in popular remote-sensing software (e.g., The Environment for Visualizing Images).

3.2 Unmanned aerial vehicle data

Unmanned aerial vehicle data were gathered from May 10 to 20, 2015. In the study area, 12 samples of ortho-mosaic images were obtained. The size of each sample UAV data was about 700 m× 800 m and the spatial resolution was 5 cm × 5 cm. The 12 samples of UAV data cover severe rocky desertification areas, moderate rocky desertification areas, and slight rocky desertification areas in Xingren County (Fig. 1). The high-resolution UAV data were used to extract the true values of the bedrock exposure rate. The main pre-processing of the UAV data was geometric correction and we used a second-order polynomial model and the SPOT6 images were used as reference image.

4 Methods

This study explored a high-precision quantitative inversion method for obtaining the bedrock exposure rate based on multi-scale remote-sensing data. Firstly, the UAV image was divided into object classes and the bedrock exposure rate was calculated at the scale of the Landsat-8 OLI pixel size. Then, using parts of the calculated samples, the band reflectivity of Landsat-8 OLI data and rock index were

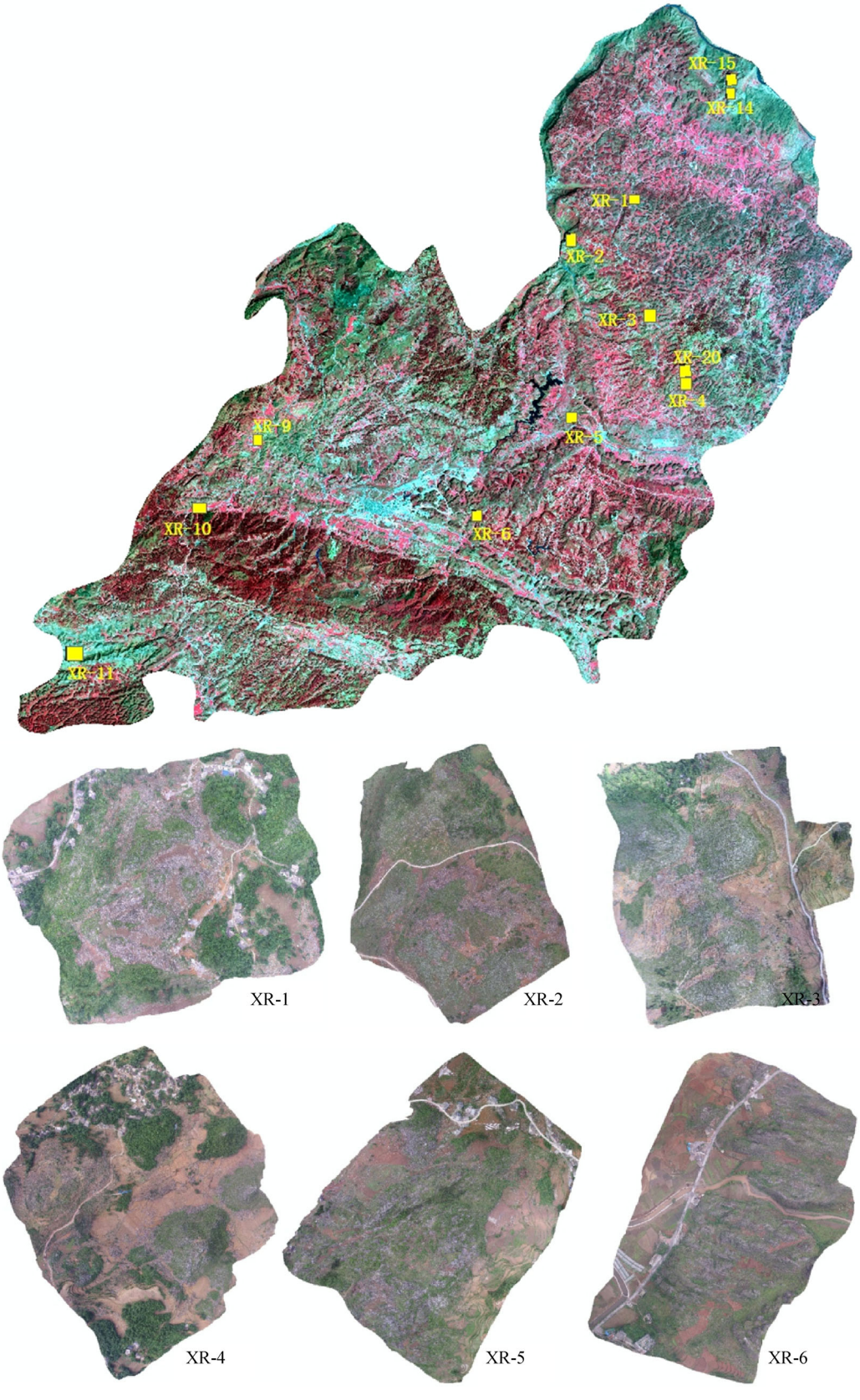
XR-15
XR-14
XR-1
XR-2
XR-3
XR-20
XR-4
XR-9
XR-5
XR-10
XR-6
XR-11
XR-1
XR-2
XR-3
XR-4
XR-5
XR-6

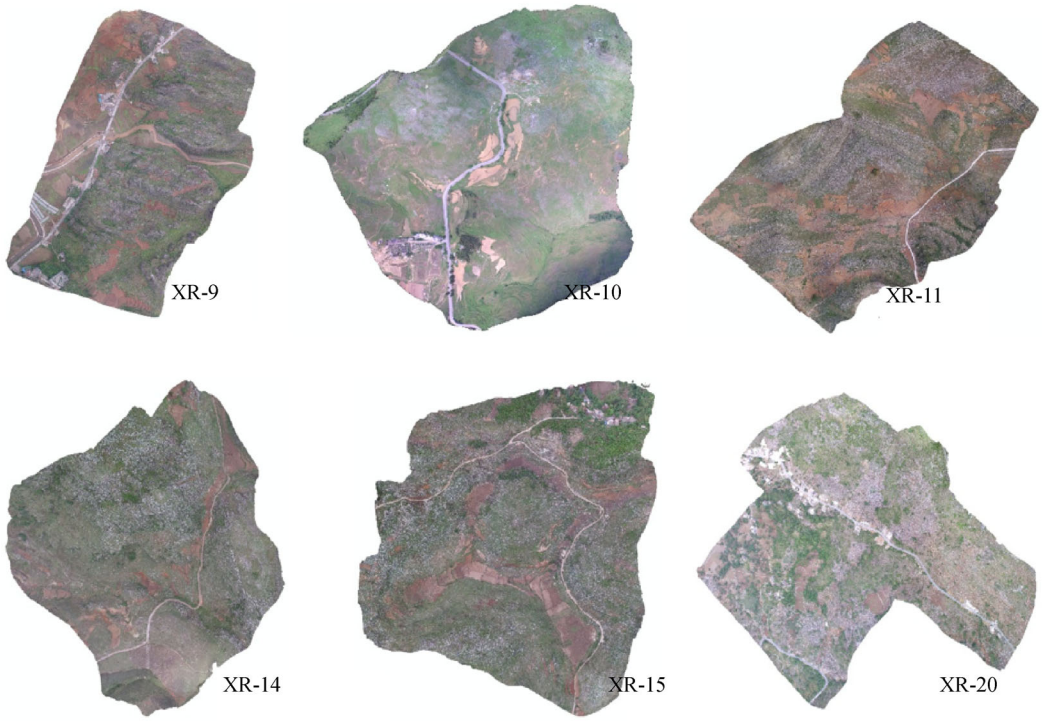

Fig. 1 Distribution of 12 samples of unmanned aerial vehicle data (Upper image). (Lower images, labelled XR-1 to XR-20) ortho-mosaic images of the study area.

used to train a back-propagation neural network. Finally, the network model was used to generate the bedrock exposure rate based on the Landsat-8 OLI image. A summary of our quantitative extraction method for the bedrock exposure rate is provided in Fig. 2.

4.1 UAV data classification and bedrock exposed rate calculation

4.1.1 Object-oriented classification of UAV data

To provide precise values of bedrock exposure rate for use in training the inversion method, five classes (rock, vegetation, road, water, and bare soil) were defined using high-resolution UAV data based on object-oriented classification. Object-based classification includes the delineation and classification of spatial units. Firstly, the UAV images were divided up. Secondly, a decision event tree based on physically interpretable thresholds of selected spectral and textural features was applied. Thirdly, calculation of segmented object attributes was conducted using the shape, texture (roughness), and spectral values. Lastly, the delineated objects were classified into rock, vegetation, road, water, and bare soil.

4.1.2 Calculation of the bedrock exposed rate

We generalized a 30-m grid exactly the same as that of the Landsat-8 OLI image and then removed the incomplete spatial grid at the edges of each UAV dataset (an example is provided in Fig. 3). Based on the results from the UAV data, we carried out statistical analysis of the rock area in each grid square, producing bedrock exposure rate datasets. These datasets were used to train the inversion method based on the Landsat-8 OLI data to produce a distribution map of the bedrock exposure rate.

$$y = \frac{A}{900}, \tag{1}$$

where y is the bedrock exposure rate of each grid square, A is the rock area in each grid square, and 900 is the total area of each grid square.

4.2 Bedrock exposure rate inversion based on Landsat-8 OLI image

4.2.1 Analysis of sensitive parameters

In this study, four types of features were selected for analysis of the sensitive parameters. The four types of features were the reflectance of each band, vegetation index, various rock indexes, and topographic factors. The features are explained in Table 1. Correlation analysis of the bedrock exposure rate and various indexes was performed to select the sensitive parameters.

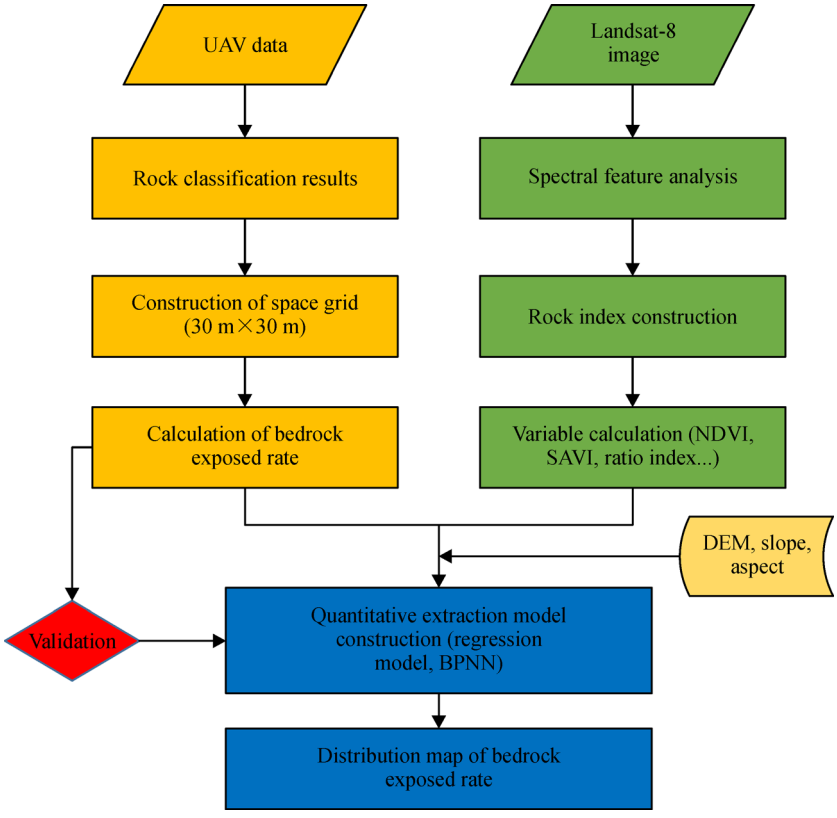

Fig. 2 Schematic diagram of the bedrock exposed rate inversion based on the UAV data and Landsat-8 OLI image.

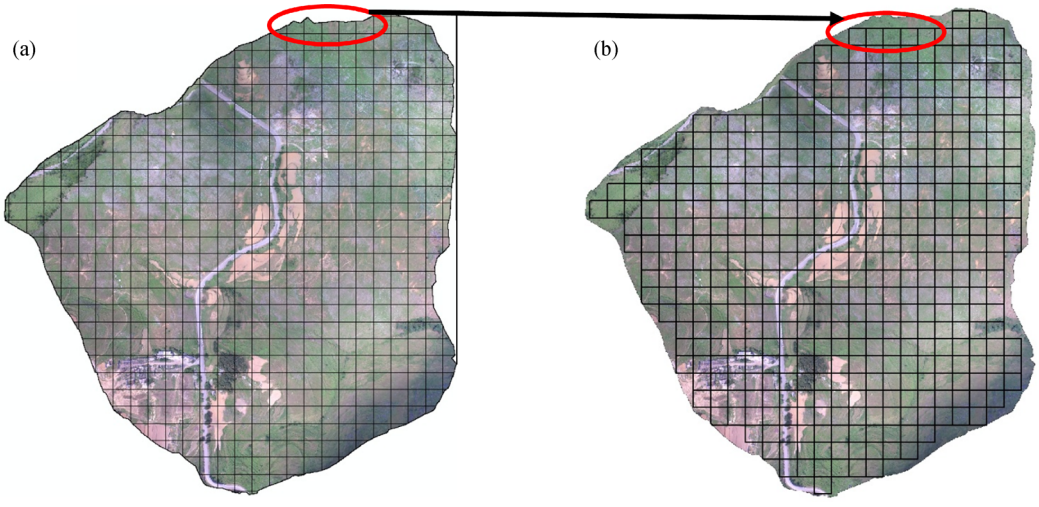

Fig. 3 Construction of a spatial grid (the incomplete spatial grids at the edges are removed in Fig. 3(b)) for one UAV dataset.

Table 1 Various indices used in this study

No.	Types	Features
1	Band reflection	b1—band2 Blue, b2—band3 Green, b3—band4 Red, b4—band5 NIR, b5—band6 SWIR1, b6—band7 SWIR2, b7—band9 Cirrus
2	Vegetation index	NDVI =(b4–b3)/(b4 + b3), SAVI =(b4–b3)/(b4 + b3 + L)(1 + L)
3	Rock index	(b7–b5)/(b7 + b5), (b7–b6)/(b7 + b6), (b6–b2)/(b6 + b2), (b6–b4)/(b6 + b4), b7/b6, b6/b5, b5/b4, b5/b3
4	Topographic factors	DEM, Slope, Slope aspect

4.2.2 Construction of an inversion model of the bedrock exposure rate using a back-projection neural network

The back-projection (BP) neural network was trained using the true values of bedrock exposure rate calculated from the UAV data and various indices based on the Landsat-8 OLI image. BP neural network is one of the most mature and widely used artificial neural network models. BP neural network has the advantages of simple structure, good self-learning capability, and effectively solves the approximation problems of nonlinear objective function, which has been widely used in image recognition, function approximation and other fields.

In this study, we used a back-propagation neural network with three layers (input, hidden, and output). In the BP neural network, seven band reflections, two vegetation indices, eight rock indices, and three topographic factors were used as input variables. The bedrock exposure rate was the output variable. There were 38 nodes in the hidden layer. The training function was trainlm, the network target error was 0.00001, the training iteration number was 1000, and the learning rate was 0.05. The training was carried out based on simple, iterative back-propagation and minimization of the Root Mean Square Error (RMSE) between the estimated bedrock exposure rate ($x_{i(\mathrm{BP})}$) and the actual rate (x_i). The procedure for the inversion model was implemented using MATLAB R2014a software.

$$\mathrm{RMSE} = \sqrt{\frac{\sum_{i=1}^{n}\left(x_{i(\mathrm{BP})} - x_i\right)^2}{n}}. \quad (2)$$

5 Results and discussion

5.1 Correlation analysis of bedrock exposed rate and various indices

In our study, 12 samples of UAV data were classified into five classes based on object-oriented classification method. Accuracy assessment were based on another pixel sets selected beforehand refer to visual interpretation samples and expert knowledge. The overall accuracy of UAV data were 90%–95%. In this study, 1937 spatial grid bedrock exposure rate data were obtained and four features were extracted from each spatial grid.

The correlations between the bedrock exposure rate and various indices were analyzed: the results are provided in Table 2. The correlation between the bedrock exposure rate and any single index is not high. The highest correlation coefficient R was about 0.64; the indices that exhibited a higher correlation with the bedrock exposure rate were b1, b2, ((b7 − b6)/(b7 + b6)), and b7/b6. This result may be because of the complexity of the karst landforms in the study area.

5.2 BP neural network inversion model construction

We obtained 1937 data samples in this study, of which 1356 (70%) were randomly selected for modelling and the remaining 581 were used for validation in the back-propagation neural network model. The 1356 data samples were trained by the network and simulation of the bedrock exposure rate was performed on the validation samples after the convergence of training. The simulation results were compared with the actual values: the results of BP neural network model training and validation are illustrated in Fig. 4. The correlation coefficient R of the BP neural network training model was 0.855, R for the validation model was 0.677, and the RMSE between the simulated and actual bedrock exposed rate was 0.073.

To compare the BP neural network, a multiple linear stepwise regression model and multiple linear regression model were constructed using the same 1356 data samples as the BP neural network training data. The other 581 samples were used for validation. The training model equations of the two regression models are shown in Table 3 and Table 4. In the validation models (Fig. 5), the simulated bedrock exposure rate showed some negative values. The R values of the multiple linear stepwise

Table 2 Correlation coefficients between bedrock exposed rate and various indices

Bedrock exposed rate	Parameter	Correlation coefficient R	Bedrock exposed rate	Parameter	Correlation coefficient R
Y	b1	0.6446	Y	NDVI	−0.5413
	b2	0.6498		SAVI	−0.4504
	b3	0.5355		(b6 − b2)/(b6 + b2)	−0.5283
	b4	0.4793		(b6 − b4)/(b6 + b4)	−0.4881
	b5	0.0196		(b7 − b5)/(b7 + b5)	0.5287
	b6	0.3400		(b7 − b6)/(b7 + b6)	0.6329
	b7	0.5107		b7/b6	0.6385
	DEM	0.0546		b6/b5	0.4268
	Slope	0.0241		b5/b3	−0.5976
	Slope aspect	0.0014		b5/b4	−0.5264

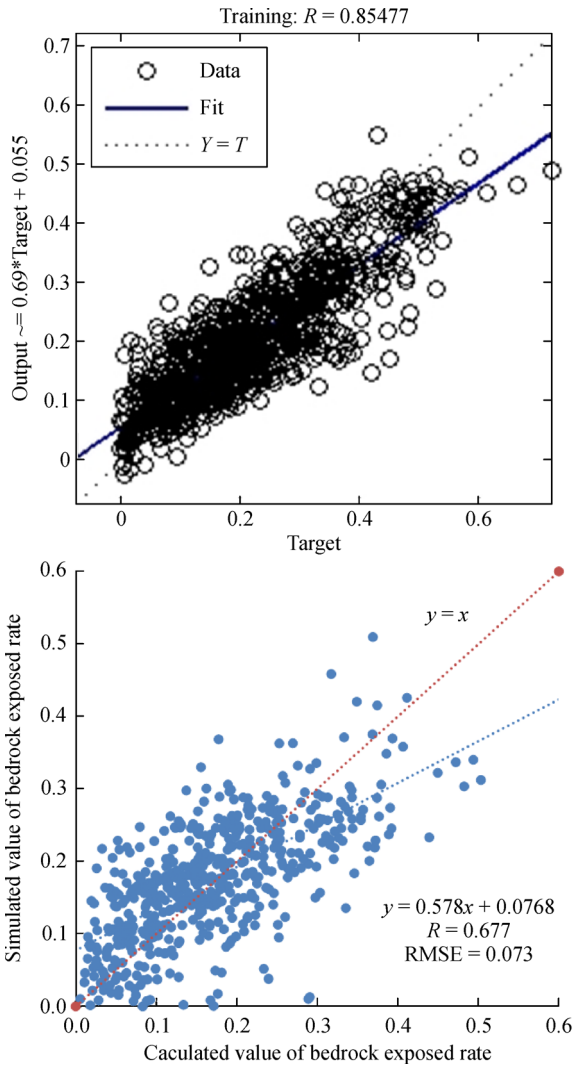

Fig. 4 Results of BP neural network model training and validation.

Table 3 The training model equation of multiple linear stepwise regression model

Parameter	Coefficient	Parameter	Coefficient
b1	−7.916	Constant	−1.812
b2	25.615	(b6−b2)/(b6+b2)	1.153
b4	−2.653	DEM	0.252
b7	−3.12	Slope	−0.001
b7/b6	1.148	Slope aspect	0.001

regression and multiple linear regression training models were 0.787 and 0.790; R values of the validation models were 0.604 and 0.614. The RMSE between the simulated and actual bedrock exposure rate was 0.088 and 0.086.

The training and verification accuracy of the BP neural network model was relatively high compared to the

Table 4 The training model equation of multiple linear regression model

Parameter	Coefficient	Parameter	Coefficient
Constant	−4.97	NDVI	2.856
b1	−6.871	SAVI	2.652
b2	17.119	(b6−b2)/(b6+b2)	0.401
b3	4.949	(b6−b4)/(b6+b4)	−2.535
b4	3.224	(b7−b5)/(b7+b5)	4.423
b5	−2.312	(b7−b6)/(b7+b6)	11.357
b6	−4.201	b7/b6	4.97
b7	0.046	b6/b5	−5.277
DEM	0.199	b5/b3	0.57
Slope	−0.119	b5/b4	−0.737
Slope aspect	−0.054		

multiple linear regression and stepwise regression methods, and the error between the simulated and actual bedrock exposure rate was small. In our study area, the linear regression model cannot extract the bedrock exposure rate very well owing to the high complexity and heterogeneity of karst environments. BP neural network has the advantages of simple structure, good self-learning capability, and effectively solving the approximation problems of nonlinear objective functions, which can be used for quantitative extraction of the bedrock exposure rate in karst areas.

5.3 BP neural network inversion model application

From the Landsat-8 OLI image of Xingren County, various indices were obtained, including the reflectance of each band, vegetation index, and rock index. By incorporating the indices data into the constructed BP neural network, the bedrock exposure rate in Xingren County was estimated and a distribution map of the bedrock exposure rate was obtained (Fig. 6). The bedrock exposure rate is higher in the northeastern, southwestern, and central parts of Xingren County: these are the areas in which rocky desertification is most serious. These areas are mainly mountainous areas in which the soil is thin, vegetation cover is low, and the soil erosion is serious. The results were consistent with the geomorphic features of Xingren County.

5.4 Discussion

In the bedrock exposure rate inversion, several factors could affect the accuracy of the bedrock exposure rate estimation.

1) Sample representation. In our study area, 12 samples of unmanned aerial vehicle data were obtained; additional unmanned aerial vehicle data for the training model might

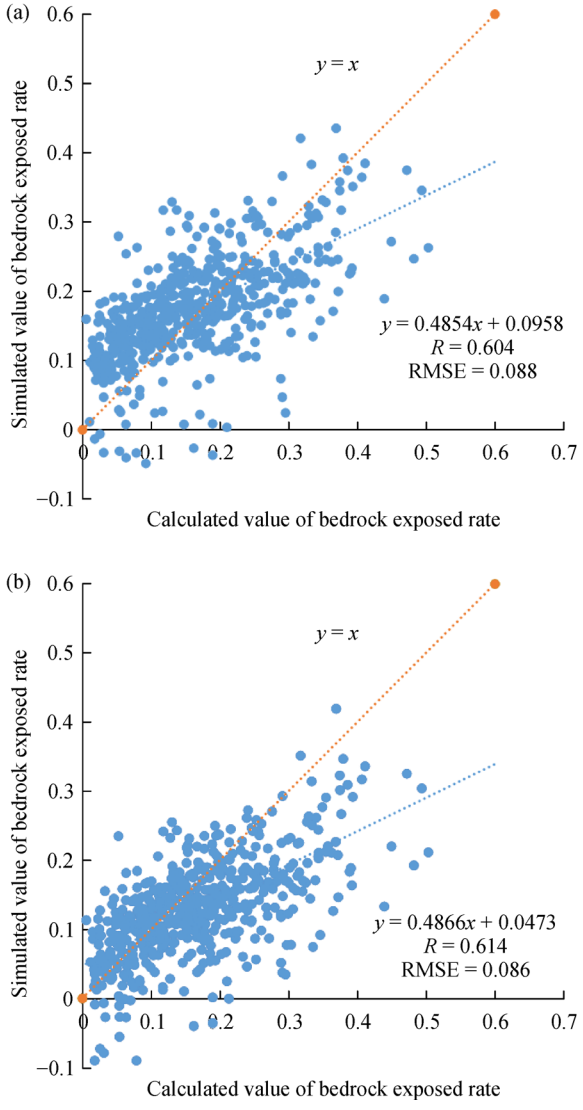

Fig. 5 Relationship between simulated and calculated bedrock exposed rate with the multiple linear stepwise regression model (a) and multiple linear regression model (b).

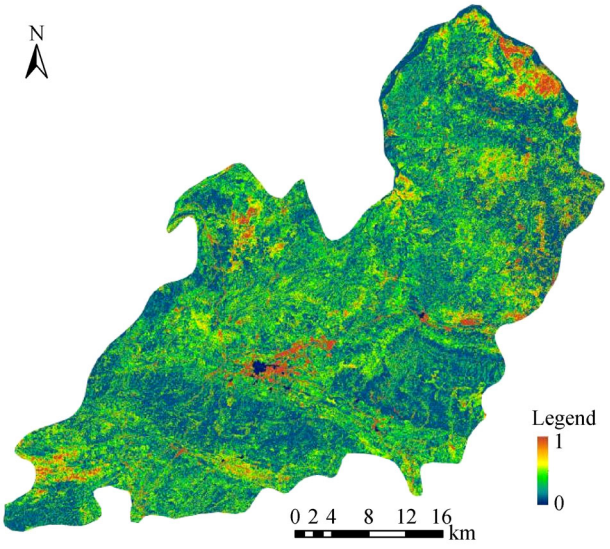

Fig. 6 Distribution of the bedrock exposed rate in Xingren County.

be required.

2) Reliability of the true value of the bedrock exposure rate. The classification quality of UAV data is an important factor affecting the true value of the bedrock exposure rate.

3) Large differences in scale. Landsat-8 OLI image and UAV data were used to extract the bedrock exposure rate. The spatial resolution of the Landsat-8 OLI data was 30 m × 30 m; that of the UAV data was 5 cm × 5 cm.

4) Complexity of mixed ground objects in spatial grids. In our study area, most of the spatial grids were mixed pixels, and the mixed pixels contained three main components: rock, bare soil, and vegetation. The complexity of the combinations of the three components (rock, bare soil, and vegetation) had a direct influence on the accuracy of the inversion model of the bedrock exposure rate. In the same grids of bedrock exposure rate, because the proportions of bare soil and vegetation were variable, the band reflectance of the Landsat-8 OLI image was different, which led to a dispersed distribution of modelling sample points and affected the accuracy of the model.

Taking XR-20 UAV data as an example, the relationship between the rock index (b7/b6) and bedrock exposure rate was analyzed (Fig. 7). When the bedrock exposure rate was relatively low, the scatter plot was more discrete, which directly reduced the model accuracy. For example, in spatial grids 60, 62, and 81 of Fig. 8, the bedrock exposure rate was relatively low. However, the proportion of vegetation was very high in spatial grid 62 and that of bare soil was higher in spatial grid 60; in addition, the rock index (b7/b6) values of these two spatial grids was very different. Although the proportion of vegetation was very high in spatial grids 62 and 81, the cover vegetation was shrub in spatial grid 62 and grass in spatial grid 81, which

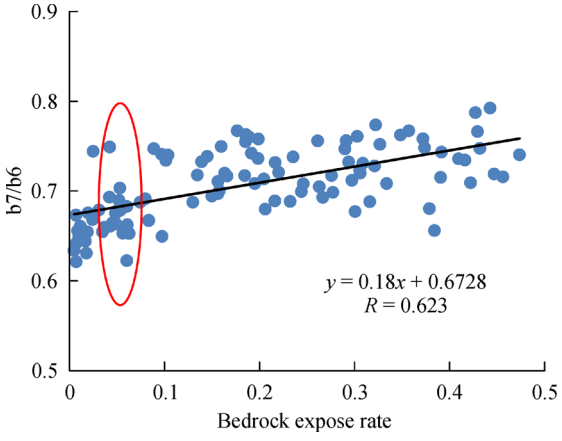

Fig. 7 Relationship between the rock index (b7/b6) and the bedrock exposed rate.

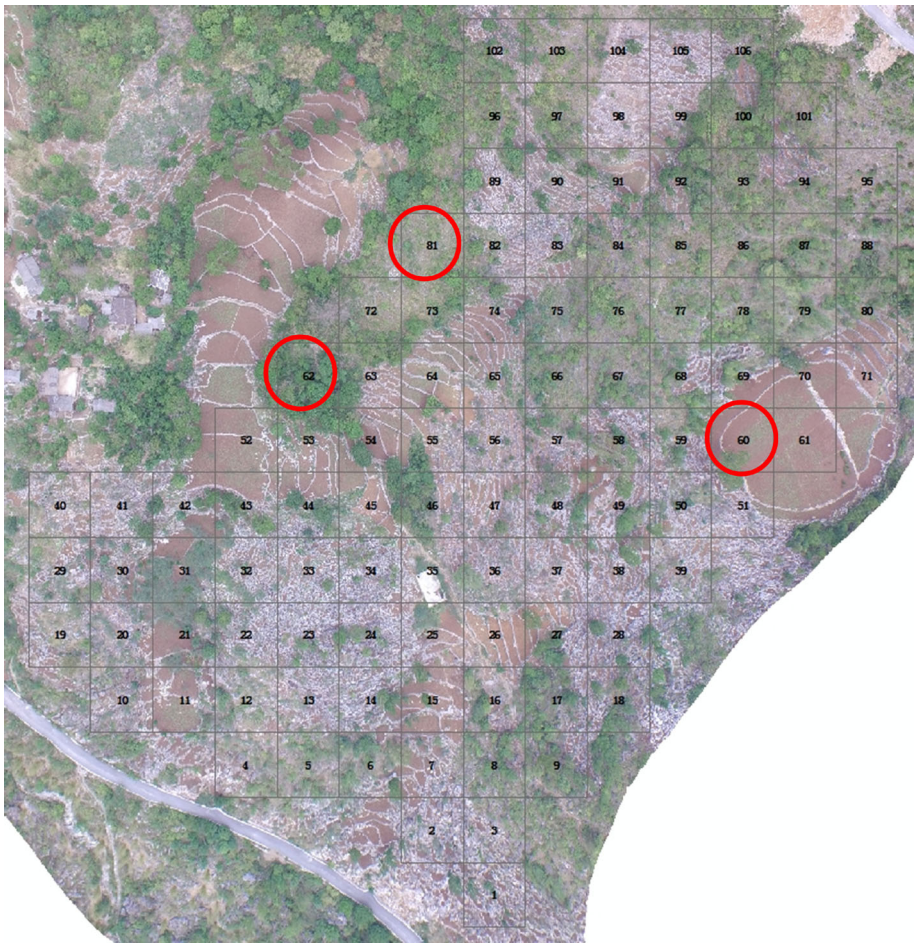

Fig. 8 Distribution of the spatial grid in XR-20 UAV data.

resulted in different rock index (b7/b6) values. Therefore, the complexity of mixed ground objects in the spatial grids was an important factor affecting the accuracy of the bedrock exposure rate inversion.

The results also demonstrate that it is possible to estimate the bedrock exposure rate accurately combining unmanned aerial vehicle data and Landsat-8 OLI images in a karst environments. In practice, when estimating the bedrock exposure rate over a large area, there should be a sampling schema for acquisition of images with high spatial resolution; in addition, a more satisfactory classification of high-spatial-resolution images is needed. This will produce more accurate values of the bedrock exposure rate to feed the BP neural network training and produce a more reliable bedrock exposure rate for the Landsat-8 OLI image, which in turn will allow more accurate estimation of the bedrock exposure rate.

In our experiment, the coverage of the acquired UAV data was somewhat small, but with the development of satellite technology, many high-resolution remote-sensing data with a spatial resolution of less than 1 m, such as GF-2, worldview-2/3, and QuickBird are available. These data can be applied to quantitative extraction of the bedrock exposure rate.

6 Conclusions

The feasibility of quantitative extraction of the bedrock exposure rate using sub-pixel methods based on unmanned aerial vehicle data and Landsat-8 OLI image performs much better at large areas in karst environments. The UAV data provided good input of bedrock exposure rate for BP neural network training. The sub-pixel method based on BP neural network training in this study provided reliable values of bedrock expossure rate and can be used operationally in karst environments.

The following preconditions should also be applied when performing quantitative extraction of the bedrock exposure rate using an operational workflow: 1) accurate high-resolution classification and 2) more high-resolution images with equal spatial distribution that allow better BP neural network training and acquisition of a more reliable bedrock exposure rate.

Acknowledgements This study was supported by the National Natural Science Foundation of China (Grant Nos. 41501467 and 41361091).

References

Dai Q, Peng X, Yang Z, Zhao L (2017). Runoff and erosion processes on bare slopes in the karst rocky desertification area. Catena, 152: 218–226

Geerken R, Ilaiwi M (2004). Assessment of rangeland degradation and development of a strategy for rehabilitation. Remote Sens Environ, 90(4): 490–504

Jiang Z, Lian Y, Qin X (2014). Rocky desertification in southwest China: impacts, causes, and restoration. Earth Sci Rev, 132(3): 1–12

Lagacherie P, Baret F, Feret J B, Netto J M, Robbez-Masson J M (2008). Estimation of soil clay and calcium carbonate using laboratory, field and airborne hyperspectral measurements. Remote Sens Environ, 112 (3): 825–835

Matthew M W, Adler-Golden S M, Berk A, Richtsmeier S C, Levine R Y, Bernstein L S, Acharya P K, Anderson G P, Felde G W, Hoke M L (2000). Status of atmospheric correction using a MODTRAN4-based algorithm. In: AeroSense 2000. International Society for Optics and Photonics, 199–207

Roy D P, Wulder M A, Loveland T R, Woodcock C E, Allen R G, Anderson M C, Helder D, Irons J R, Johnson D M, Kennedy R, Scambos T A, Schaaf C B, Schott J R, Sheng Y, Vermote E F, Belward A S, Bindschadler R, Cohen W B, Zhu Z (2014). Landsat-8: science and product vision for terrestrial global change research. Remote Sens Environ, 145(145): 154–172

Runnström M C (2003). Rangeland development of the Mu Us Sandy Land in semiarid China: an analysis using Landsat and NOAA remote sensing data. Land Degrad Dev, 14(2): 189–202

Salvati L, Kosmas C, Kairis O, Karavitis C, Acikalin S, Belgacem A, Solé-Benet A, Chaker M, Fassouli V, Gokceoglu C, Gungor H, Hessel R, Khatteli H, Kounalaki A, Laouina A, Ocakoglu F, Ouessar M, Ritsema C, Sghaier M, Sonmez H, Taamallah H, Tezcan L, de Vente J, Kelly C, Colantoni A, Carlucci M (2016). Assessing the effectiveness of sustainable land management policies for combating desertification: a data mining approach. J Environ Manage, 183: 754–762

Tavares J D P, Baptista I, Ferreira A J D, Amiotte-Suchet P, Coelho C, Gomes S, Amoros R, Reis E A D, Mendes A F, Costa L, Bentub J, Varelaet L (2015). Assessment and mapping the sensitive areas to desertification in an insular sahelian mountain region case study of the ribeira seca watershed, Santiago Island, Cabo Verde. Catena, 128: 214–223

Wang S J, Li Y B (2007). Problems and development trends about researches on karst rocky desertification. Advances in Earth Science, 22(6): 573–582 (in Chinese)

Xie X, Du P, Xia J, Luo J (2015). Spectral indices for estimating exposed carbonate rock fraction in karst areas of southwest China. IEEE Geosci Remote Sens Lett, 12(9): 1988–1992

Xiong Y, Yue Y M, Wang K L (2013). Comparative study of indicator extraction for assessment of karst rocky desertification based on hyperion and ASTER images. Bulletins of Soil and Water Conservation, 33(3): 186–190 (in Chinese)

Xu E Q, Zhang H Q (2014). Characterization and interaction of driving factors in karst rocky desertification: a case study from Changshun, China. Solid Earth, 5(2): 1329–1340

Yang Q Y, Jiang Z C, Ma Z L, Luo W Q, Yin H, Yu Q W, Li W J (2012). Spatial variability of karst rock desertification based on geostatistics and remote sensing. Transactions of the Chinese Society of Agricultural Engineering, 28(4): 243–247 (in Chinese)

You H (2017). Orienting rocky desertification towards sustainable land use: an advanced remote sensing tool to guide the conservation policy. Land Use Policy, 61: 171–184

Yue Y, Zhang B, Wang K, Ru L I, Liu B, Zhang M (2011). Remote sensing of indicators for evaluating karst rocky desertification. Journal of Remote Sensing, 15(4): 722–736

Yue Y M, Wang K L, Zhang B, Jiao Q J, Liu B, Zhang M Y (2012). Remote sensing of fractional cover of vegetation and exposed bedrock for karst rocky desertification assessment. Procedia Environ Sci, 13(10): 847–853

Zhang M Y, Wang K L, Zhang C H, Chen H S, Liu H Y, Yue Y M, Luffman I, Qi X K (2011). Using the radial basis function network model to assess rocky desertification in northwest Guangxi, China. Environ Earth Sci, 62(1): 69–76

Zhang X, Shang K, Cen Y, Shuai T, Sun Y L (2014). Estimating ecological indicators of karst rocky desertification by linear spectral unmixing method. Int J Appl Earth Obs Geoinf, 31(9): 86–94

Zhang Z, Ouyang Z, Xiao Y, Xiao Y, Xu W (2017). Using principal component analysis and annual seasonal trend analysis to assess karst rocky desertification in southwestern China. Environ Monit Assess, 189(6): 269

Zong H L, Gan S, Ren P F (2014). Research on extraction of karst rocky desertification information in southeastern Yunnan. Value Engineering, 1(10): 211–214 (in Chinese)